Volume 3
Number 14
21 July 2021
Pages 3969–4294

Nanoscale Advances

rsc.li/nanoscale-advances

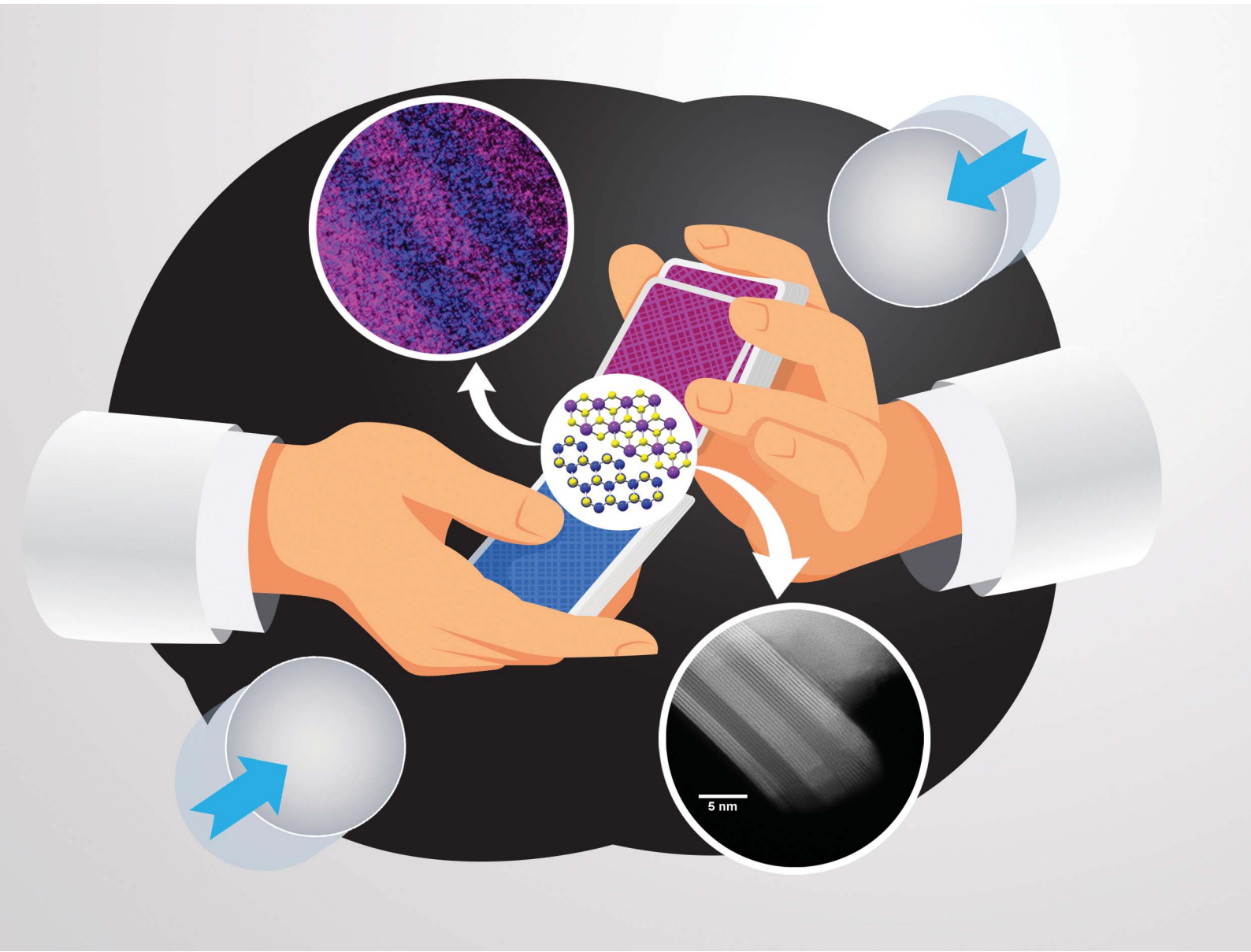

ISSN 2516-0230

ROYAL SOCIETY OF CHEMISTRY

PAPER
Ihor Z. Hlova, Viktor P. Balema *et al.*
Incommensurate transition-metal dichalcogenides *via* mechanochemical reshuffling of binary precursors

NCNST

Nanoscale Advances

ROYAL SOCIETY OF CHEMISTRY

PAPER

View Article Online
View Journal | View Issue

Cite this: *Nanoscale Adv.*, 2021, **3**, 4065

Incommensurate transition-metal dichalcogenides *via* mechanochemical reshuffling of binary precursors†

Ihor Z. Hlova,‡*[a] Prashant Singh,‡[a] Serhiy Z. Malynych,[b] Roman V. Gamernyk,[c] Oleksandr Dolotko,[a] Vitalij K. Pecharsky,[ad] Duane D. Johnson,[ad] Raymundo Arroyave,[e] Arjun K. Pathak[f] and Viktor P. Balema*[a]

Received 23rd January 2021
Accepted 6th June 2021

DOI: 10.1039/d1na00064k

rsc.li/nanoscale-advances

A new family of heterostructured transition-metal dichalcogenides (TMDCs) with incommensurate ("misfit") spatial arrangements of well-defined layers was prepared from structurally dissimilar single-phase 2H-MoS_2 and 1T-HfS_2 materials. The experimentally observed heterostructuring is energetically favorable over the formation of homogeneous multi-principle element dichalcogenides observed in related dichalcogenide systems of Mo, W, and Ta. The resulting three-dimensional (3D) heterostructures show semiconducting behavior with an indirect band gap around 1 eV, agreeing with values predicted from density functional theory. Results of this joint experimental and theoretical study open new avenues for generating unexplored metal-dichalcogenide heteroassemblies with incommensurate structures and tunable physical properties.

1 Introduction

Layered transition-metal dichalcogenides (TMDCs) with a chemical formula of MX_2, where M is a group 4–6 refractory metal and X is a chalcogen (S, Se, or Te), continue to receive much attention as easily accessible sources of single-layer 2D-nanomaterials and building blocks for 3D-heterostructures that demonstrate a broad variety of physical properties suitable for diverse applications.[1–7] Generally, heterostructured materials are formed as a result of elaborate syntheses and in minuscule quantities. A versatile synthetic approach enabling simple and reliable preparation of 3D-heterostructured TMDCs in bulk will make those materials broadly available for both fundamental and applied research, potentially revealing new physics and new areas for applications.

Bulk TMDCs are built from layers of covalently bonded metal and chalcogen atoms held together *via* weak van der Waals (vdW) forces (see ESI, Fig. S1†). As a result, they can be easily exfoliated into 2D-nanosheets, even down to single layers.[8] Both bulk and 2D-TMDCs demonstrate a broad range of electronic transport properties that span from indirect and direct gap semiconductivity, semimetallic and metallic behavior, to low-temperature superconductivity, depending on the chemical composition and the spatial configurations of the material as well as external stimuli applied.[1,9]

While binary TMDCs are well known,[10] the preparation of layered multi-principal element metal chalcogenides, where different metals (M) and chalcogens (X) share a common crystal lattice, remained challenging until our recent report.[11] One of the intriguing outcomes of this earlier study was the observed heterostructuring of different group 5 and 6 binary TMDCs upon mechanical milling at room temperature. Thus-produced 3D-heterostructures are metastable and, when subjected to high-temperature annealing, they transform into uniform single-phase materials. However, if the starting metal chalcogenides possess different crystal structures and stoichiometries, *e.g.* TaS_2 and SmS, or $NbSe_2$ and LaSe, under similar processing conditions they form well-defined and thermodynamically stable heterostructures with incommensurate (misfit) spatial arrangements, where slabs of the mono-chalcogenide (SmS or LaSe) with cubic crystal structures alternate with hexagonal 2D layers of the TMDC (TaS_2 or $NbSe_2$).[12]

The latter discovery raised questions about possibility to design layered misfit materials from chemically related yet structurally dissimilar building blocks, such as hexagonal 2H-

[a]*Ames Laboratory, U.S. Department of Energy, Iowa State University, Ames, IA, 50011-2416, USA. E-mail: vbalema@ameslab.gov; ihlova@ameslab.gov*
[b]*Hetman Petro Sahaidachnyi National Army Academy, Lviv, 79026, Ukraine*
[c]*Ivan Franko National University of Lviv, Lviv, 79005, Ukraine*
[d]*Department of Materials Science and Engineering, Iowa State University, Ames, IA, 50011-1096, USA*
[e]*Department of Materials Science & Engineering, Texas A&M University, College Station, TX, 77843, USA*
[f]*Department of Physics, SUNY Buffalo State, Buffalo, NY, 14222, USA*

† Electronic supplementary information (ESI) available: Additional experimental details on precursor synthesis, Rietveld refinement, photoconductivity and magnetoresistance measurements, and density functional theory calculations. See DOI: 10.1039/d1na00064k

‡ These authors contributed equally.

MoS_2 [13] and trigonal 1T-HfS_2,[14] by their simultaneous mechanochemical exfoliation and re-assembly into TMDCs heterostructures. If feasible, this would open a new avenue to an unexplored family of incommensurate 3D-heterostructures with tunable physical properties. Below we report on the successful implementation of this idea.

2 Experimental

2.1 Synthesis of 3D-heterostructures

In a standard experiment, 3 g of a mixture of MoS_2 and HfS_2 (see ESI, and Fig. S2†) weighed in a desired stoichiometric ratio was loaded in a zirconia vial together with five 12.7 mm zirconia balls. To prevent oxidation. All operations were conducted under the inert atmosphere of an argon-filled glovebox. The sample was milled for 30 hours in a planetary mill (Fritsch, Pulverisette 7) and transferred back to the argon-filled glovebox for loading into a quartz ampule. The ampule was sealed under ultra-high purity helium and the sample was annealed for 3 days at 1000 °C. Thereafter it was cooled down to room temperature and transferred back to the glovebox for further handling.

2.2 Powder X-ray diffraction (PXRD)

Phase analyses and structural characterizations of all reactions products were carried out by powder X-ray diffraction (XRD) at room temperature on a PANalytical powder diffractometer using Cu-Kα radiation in the range of Bragg angles $10^\circ \leq 2\theta \leq 80^\circ$ with a 0.02° step. Considering lack of periodicity along the stacking direction of a few nanometer thick slabs of the constituent phases, unavoidable and strong texturing, and highly anisotropic peak broadening, Rietveld refinement was impossible. Hence, Le Bail refinements (see ESI and Fig. S3† as an example) of the lattice parameters of the individual phases were performed using FullProf sofware.[15] The backgrounds were fitted by linear interpolations between selected data points in the regions with no Bragg peaks present. The pseudo-Voigt function was used to approximate peak shapes, with peak shape parameters refined separately for each of the two phases present.

2.3 Scanning transmission electron microscopy (STEM)

High-angle annular dark-field (HAADF) scanning transmission electron microscopy (STEM) and energy dispersive X-ray spectrometry (EDS) experiments were performed on a Titan Themis (FEI) probe Cs-corrected TEM. The high-resolution HAADF-STEM imaging was carried out using a convergence semi-angle of 18 mrad and a collection semi-angle of 99–200 mrad at 200 kV. STEM-EDS analysis was performed using a Super-X EDS detector attached to the Titan Themis.

2.4 Band gap measurements

Optical measurements were performed using a custom-built experimental setup (ESI, and Fig. S4† for further details) based on a diffractive monochromator (focal length of the lens 600 mm). A quartz halogen lamp was utilized as a light source and a photomultiplier tube (PMT) was used to detect the radiation. Samples were placed inside the integrating sphere and their diffuse reflectance spectra (DRS) were recorded. Barium sulphate served as a standard. The acquired DRS were converted to Kubelka–Munk function (absorption-to-scattering ratio α/S).

2.5 Density functional theory calculations

Density Functional Theory (DFT) calculations were employed as implemented in the Vienna *ab initio* simulations package (VASP)[16–18] with Projector Augmented Wave (PAW) method.[19,20] The plane-wave basis cut-off was set at 500 eV, and the *k*-mesh to sample the first Brillouin zone for geometry optimization and band structure were, respectively, $5 \times 5 \times 1$ and $7 \times 7 \times 2$. Unit-cell translation vectors, cell volumes, and atomic positions were fully optimized in the heterostructures and single-phase solid solution (SS) materials. The convergence criteria for the residual force and energy were set to 10^{-3} eV Å^{-1} and 10^{-5} eV per atom, respectively. The parameter-free van der Waals density functional (optB88-vdW)[21] was employed to account for dispersive interactions,[22] whereas the hybrid Heyd–Scuseria–Ernzerhof[23] functional was employed for band-gap calculations as the van der Waals functionals have a minor effect on the band structure.[24] Two main structural configurations that are common for transition-metal dichalcogenides, namely 2H-MX_2 and 1T-MX_2 polytypes,[1] are used to assess the formation energies of different heterostructured and single-phase materials.

For DFT calculations of $(Mo_{0.5}W_{0.5})S_2$ and $(Mo_{0.5}W_{0.5})(S_{0.5}Se_{0.5})_2$, we used (I) 24-atom supercell ($2 \times 2 \times 1$ unit cells of 2H-MoS_2) to mimic disorder, whereas 2H-MoS_2 was used to model $1 \times 1 \times 4$ heterostructure supercell. For disorder cases: we use $5 \times 5 \times 1$ and $11 \times 11 \times 5$ *k*-mesh for structural relaxation and energy. For heterostructures: we use $3 \times 3 \times 1$ and $11 \times 11 \times 1$ *k*-mesh for structural relaxation and energy. For $(Mo_{40}W_{40}Ta_{20})S_2$, (II) a 96-atom supercell ($4 \times 4 \times 1$ unit cells of 2H-MoS_2) was used to mimic disorder, whereas $1 \times 1 \times 10$ supercell of 2H-MoS_2 was used to model an ordered 4(TaS_2):8(MoS_2):8(WS_2) heterostructure. For disorder case: we use $5 \times 5 \times 3$ and $8 \times 8 \times 6$ *k*-mesh for structural relaxation and energy. For heterostructures: we use $3 \times 3 \times 1$ and $9 \times 9 \times 1$ *k*-mesh for structural relaxation and energy. A manual stacking approach was used to create vertical vdW heterostructures of 2H-MoS_2 and 1T-HfS_2 in the present study.

3 Results and discussion

3.1 Synthesis and characterization

In contrast to the mixtures of binary MX_2, where M = Mo, W, Ta, Nb, and X = S or Se, that yield single-phase TMDCs upon mechanical milling and subsequent annealing,[11] ball milling of an equimolar mixture of HfS_2 and MoS_2 in a planetary mill (Fritsch, Pulverisette 7) for 30 hours, followed by a high-temperature annealing at 1000 °C for 72 hours, does not produce a single-phase $(Mo_{0.5}Hf_{0.5})S_2$. While the X-ray diffraction (XRD) pattern of the as-milled powder consists of several broad peaks characteristic of a highly disordered solid (Fig. 1a), the material obtained after the subsequent annealing is

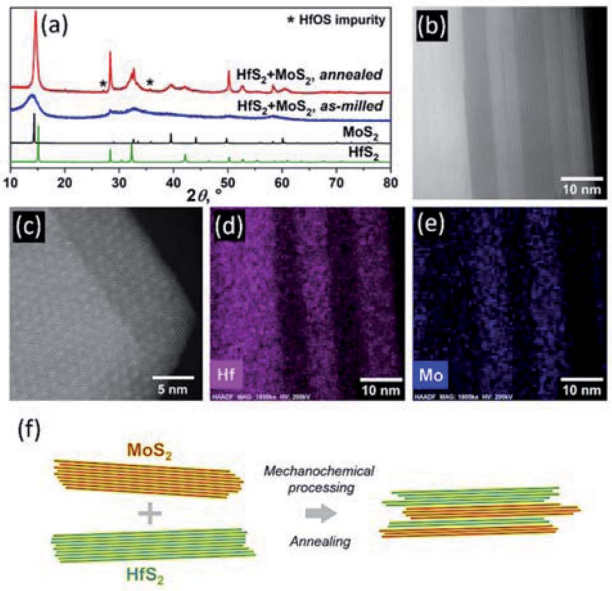

Fig. 1 (a) Powder XRD patterns of an equimolar mixture of HfS_2 and MoS_2 after ball-milling in a planetary mill for 30 hours and subsequent annealing at 1000 °C for 72 hours. XRD patterns of pure HfS_2 and MoS_2 are shown as references. Bragg peaks corresponding to an oxysulfide impurity {HfOS} are indicated by asterisks. (b) HAADF-STEM and (d, e) STEM-EDS images of the same material. Due to higher Z-contrast, HfS_2 fragments produce brighter shades, while MoS_2 layers appear as dark slabs. (c) The Moiré pattern on the surface of another, differently oriented particle of the same material. (f) Schematic diagram illustrating the formation of 3D-heterostructured TMDCs.

composed of the distinguishable HfS_2 and MoS_2 phases (Table 1, Fig. 1a).

Lattice parameters of both TMDC phases in the annealed sample reveal a slight reduction (~1.4%) of the parameter c in the MoS_2 phase and a smaller but noticeable expansion (~0.5%) of the parameter c in the HfS_2 constituent. Considering that r_{Mo} = 1.400 Å < r_{Hf} = 1.580 Å (metallic radii for coordination number 12), these anomalies cannot be attributed to minor substitutions on the metal sites. The changes that occur in opposite direction are not likely to be related to various concentrations of defects in two different structural motifs and, therefore, we ascribe them to large errors that arise from a number of factors. These are: strong diffuse scattering due to a few-nanometer thick slabs stacked along the c direction (see Fig. 1b–e); heavy overlap of the majority of the strongest Bragg peaks; and highly anisotropic broadening due to epitaxial strains that are unavoidable and cannot be removed by annealing. All of them combined, Le-Bail-refined unit-cell dimensions, and in particular those parallel to the stacking direction, become susceptible to random errors, even though the formal least squares standard deviations listed in Table 1 are low.

A minor impurity detected in the annealed sample almost certainly belongs to an off-stoichiometric hafnium oxysulfide that has formed in the sample even though all operations were carried out under high-purity argon or helium. The annealed material was further studied using High-Angle Annular Dark Field Scanning Transmission Electron Microscopy (HAADF-STEM) and Energy Dispersive Spectroscopy (STEM-EDS), which reveal a well-defined sandwich-like arrangement of the separate phases in the material as shown in Fig. 1b. The alternating phases have different Z-contrast, whereby the MoS_2 slabs appear dark and HfS_2 produces much brighter segments. The thickness of specific slabs varies, indicating stochastic nature of the mechanical exfoliation and self-assembly processes. Furthermore, the HAADF-STEM images reveal the presence of the Moiré pattern on the surface of the material (Fig. 1c), which is characteristic for TMDCs with lattice mismatch layers positioned on the top of each other,[25] *i.e.* incommensurate structural arrangements. STEM-EDS (Fig. 1d, e) confirms the 3D-heterostructured arrangement of the layers in the sample. The schematic diagram illustrating the formation of 3D-heterostructured TMDCs is shown in Fig. 1f.

Reprocessing of the annealed material by its milling for additional 30 hours, followed by annealing at 1000 °C for 72 hours, does not eliminate the phase separation in the sample.

Table 1 Lattice parameters of the 3D-heterostructured TMDCs derived from the Rietveld refinements of the corresponding powder XRD patterns[a]

MoS_2 : HfS_2 molar ratio	MoS_2 (2H) lattice parameters[b] (Å)	HfS_2 (1T) lattice parameters[c] (Å)	R_p, %
1 : 0	a = 3.160(1) Å c = 12.298(2) Å	—	6.07
0.75 : 0.25	a = 3.157(1) Å c = 12.286(1) Å	a = 3.626(1) Å c = 5.852(1) Å	7.83
0.5 : 0.5	a = 3.162(1) Å c = 12.124(1) Å	a = 3.634(1) Å c = 5.880(1) Å	7.68
0.5 : 0.5[d]	a = 3.159(1) Å c = 12.074(1) Å	a = 3.629(1) Å c = 5.881(1) Å	6.01
0.25 : 0.75	a = 3.163(1) Å c = 12.255(1) Å	a = 3.634(1) Å c = 5.951(1) Å	6.52
0 : 1	—	a = 3.628(1) Å c = 5.854(1) Å	9.88

[a] The R_p values correspond to the profile residuals. [b] Space group symmetry $P6_3/mmc$ (#194). [c] Space group symmetry $P\bar{3}m1$ (#164). [d] Processed twice using the same synthesis protocol as the previous material.

Its XRD, HAADF-STEM and STEM-EDS analyses clearly indicate that the sandwich-like arrangement of the MoS_2 and HfS_2 slabs is retained in the reprocessed material (Fig. 2, Table 1), although the slabs become markedly thinner.

Two other MoS_2-HfS_2 compositions that are rich in one or another component were prepared and investigated as well.

The XRD patterns and the structural parameters of the obtained samples are shown in Fig. 3 and Table 1. Also, in these cases, a distinctive formation of solid solutions could not be detected. The increased fraction of the HfOS impurity seen in the XRD pattern of $Hf_{0.75}Mo_{0.25}S_2$ correlates with increased concentration of Hf in the material and indicates higher sensitivity of the Hf-rich material to oxygen. As discussed above, minor non-systematic changes in the c lattice parameters are related to contributions from diffuse scattering and varying anisotropic peak broadening.

3.2 Density functional theory calculations

To gain initial insight into different chemical behaviours of structurally similar group 4, 5 and 6 TMDCs, we analysed phase stability, nature of band gap, and electronic structure calculated from DFT.

Phase stability and electronic-structure of the 2H-MoS_2:1T-HfS_2 heterostructure. An evaluation of the stable ground-state structures was carried out for two possible atomic arrangements – the heterostructure (I), where Mo and Hf are confined to separate parts of the supercell, see Fig. 4, and the solid solution (II) with statistical distribution of Hf and Mo throughout the supercell. Additional assemblies, like m(1T-HfS_2)/n(1T-MoS_2) and m(2H-HfS_2)/n(1T-MoS_2), were also considered. The number of layers in HfS_2 and MoS_2 fragments were consistently kept at $m/n = 5/5$ ratio for the equimolar chemical compositions, or $m/n = 5x/5y$ for other $x$$HfS_2$/$y$$MoS_2$ materials.

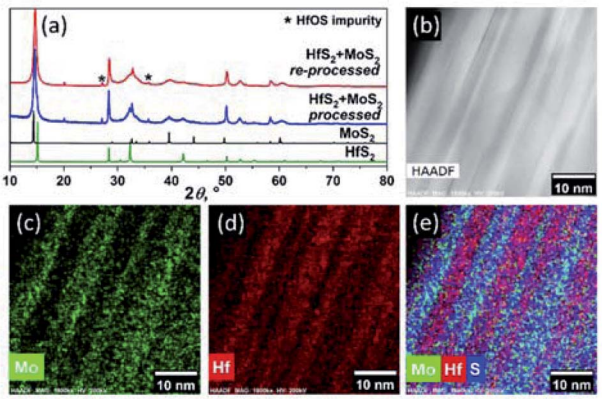

Fig. 2 (a) XRD powder patterns, (b) HAADF-STEM and (c–e) STEM-EDS images of the ball-milled sample of an equimolar mixture of HfS_2 and MoS_2 in a planetary mill for 30 hours and subsequent annealing at 1000 °C for 72 hours, followed by reworking of the material formed using the same processing protocol. XRD patterns of HfS_2 and MoS_2 are shown as references. Bragg peaks of {HfOS} impurity are indicated by asterisks.

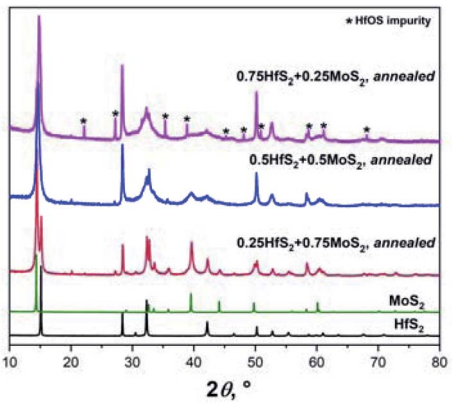

Fig. 3 The XRD patterns of different mixtures of HfS_2 and MoS_2 ball milled in a planetary mill for 30 hours and subsequent annealing at 1000 °C for 72 hours. XRD patterns of starting materials HfS_2 and MoS_2 are shown as references. The Bragg peaks of an oxysulfide impurity {HfOS} are indicated by asterisks.

The formation energies (E_{form}) calculated for equimolar. (5 : 5) HfS_2/MoS_2 heterostructures and the solid-solution (SS) compound are shown in Fig. 4c. Their comparison indicates that the 5(1T-HfS_2)/5(2H-MoS_2) arrangement is the most stable among evaluated structures, as its E_{form} is as low as −1.0902 eV per atom [which is 59.92, 73.45, and 84.32 meV below the E_{form} calculated, respectively, for 5(1T-HfS_2)/5(1T-MoS_2), 5(2H-HfS_2)/5(2H-MoS_2), and SS-($Mo_{0.5}Hf_{0.5}$)S_2].

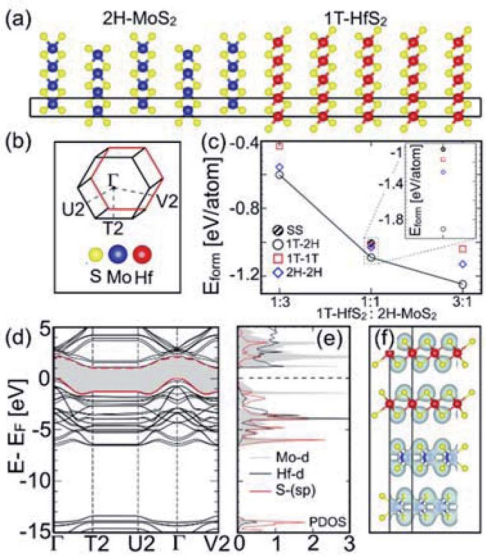

Fig. 4 (a) Atomic arrangements in 5(1T-HfS_2)/5(2H-MoS_2) heterostructure. (b) The first Brillouin zone is shown in (d). Sulphur atoms (S) are represented by yellow circles, Mo atoms are coloured blue, and Hf atoms are red. (c) Formation energies (eV per atom) of 5(1T-HfS_2)/5(2H-MoS_2) [denoted 1T/2H], 5(1T-HfS_2)/5(1T-MoS_2) [denoted 1T/1T] and 5(2H-HfS_2)/5(2H-MoS_2) [denoted 2H/2H] heterostructure, along with the ($Mo_{0.5}Hf_{0.5}$)S_2 solid-solution [denoted SS] arrangements. (d) Electronic band-structure, (e) partial density of states (states/eV-atom), and (f) charge-density distribution in the 5(1T-HfS_2)/5(2H-MoS_2) heterostructure Calculated indirect band gap is 1.01 eV and the charge-density iso-surfaces (set to 0.08 eV $Å^{-1}$) are plotted.

In addition, two other families of $x5HfS_2/y5MoS_2$ materials were investigated. Their unit cells were built from five-layer HfS_2 and MoS_2 slabs taken in $1:3$ $(x=1, y=3)$ and $3:1$ $(x=3, y=1)$ stoichiometric proportions or SS, $(Mo_yHf_x)S_2$, layers. The calculated E_{form} values are plotted in Fig. 4c. Here, we also find that the $x5(1T\text{-}HfS_2)/y5(2H\text{-}MoS_2)$ heterostructural arrangements are the most energy favorable among other evaluated cases. We also investigated several other possibilities, for example, solubility of Hf in 2H-MoS_2 or Mo in 1T-HfS_2 or anti-site defects (Mo and Hf at the interface were interchanged to see the effects on energetics), vacancies (Mo or Hf or S). However, none of these possibilities are thermodynamically stable compared to pure 2H-MoS_2-1T-HfS_2 interface.

The calculated partial density of states (DOS) and the charge-density for $5(1T\text{-}HfS_2)/5(2H\text{-}MoS_2)$ heterostructures, and the Mo-d, Hf-d, and S-sp bands are shown in Fig. 4d–f. The bands near the Fermi energy (E_F in Fig. 4d-e) mainly consist of the S-p states that are hybridized with the Mo-d and Hf-d states, whereas the S-s orbitals emerge way below E_F, and are separated from the other valence states by 8.0 eV, *i.e.*, are chemically inactive. The strong intralayer hybridization between the d-orbitals of Mo and Hf, and the p-orbitals of S is also evident from the overlapping charge densities shown in Fig. 4f, which stabilizes the $5(1T\text{-}HfS_2)/5(2H\text{-}MoS_2)$ heterostructure. The charge density in both 1T-HfS_2 and 2H-MoS_2 layers is localized on the S atoms with the directional intralayer bonding toward Mo and Hf and the band gap of 1.01 eV.

Phase stability and electronic structure of other group 5 and 6 mixed TMDCs. We have also evaluated the phase stability and electronic structures of some other group 6 TMDCs prepared and described elsewhere.[11] Further details of our calculations are shown in the ESI,† file. The calculated E_{form} of the material with overall $(Mo_{0.5}W_{0.5})S_2$ chemical composition in the SS or heterostructure states differ by more than 0.01 eV per atom in the favour of SS (−0.845 eV per atom *vs.* −0.833 eV per atom). Replacement of S by Se in $(Mo_{0.5}W_{0.5})SSe$ further destabilizes the hypothetical heterostructured arrangement and makes the formation of SS inevitable, in line with earlier experimental data.[11] The electronic band-structure, partial density of states, and charge density for $(Mo_{0.5}W_{0.5})S_2$ and $(Mo_{0.5}W_{0.5})SSe$ materials are displayed in Fig. 5.

The calculated band gaps for $(Mo_{0.5}W_{0.5})S_2$ and $(Mo_{0.5}W_{0.5})SSe$ are 1.02 eV and 1.17 eV, respectively. They are indirect in nature and follow the Γ–R high-symmetry direction. Surprisingly, the effect of Se-substitution is quite moderate in this case.

Finally, we also evaluated the formation energies and electronic structures of the single-phase material with the nominal composition of $(Mo_{0.4}W_{0.4}Ta_{0.2})S_2$. Partial replacement of Mo and W by Ta in $(Mo_{0.5}W_{0.5})S_2$ can be seen as an injection of 0.2 holes per molecule into the system. Once again, the calculated E_{form} of the "hole-doped" $(Mo_{0.4}W_{0.4}Ta_{0.2})S_2$ is substantially lower than that of the heterostructure material (−0.875 *vs.* −0.835 eV per atom), which explains the experimentally observed formation of the solid-solution phase in this case.[11]

The band structure and partial DOS for $(Mo_{0.4}W_{0.4}Ta_{0.2})S_2$ are shown in Fig. 6. The presence of Ta is responsible for only a partial filling of bonding Mo/W d-states, while they are

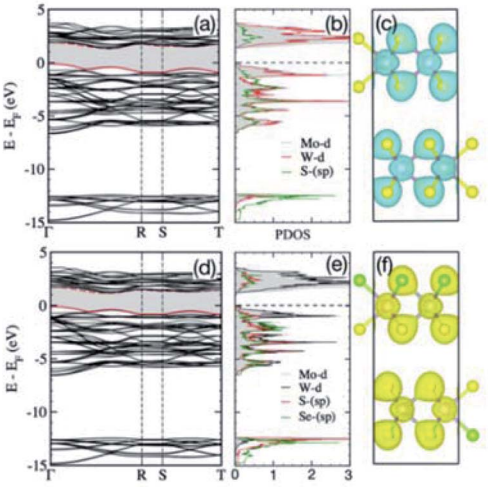

Fig. 5 Electronic band-structure, partial densities of states (states/eV-atom), and charge-density iso-surfaces (set to 0.08 eV $Å^{-1}$) of $(Mo_{0.5}W_{0.5})S_2$, (a–c) and $(Mo_{0.5}W_{0.5})SSe_2$ (d, e), respectively. The indirect band gaps were calculated at 1.02 eV for $(Mo_{0.5}W_{0.5})S_2$ and 1.17 eV for $(Mo_{0.5}W_{0.5})SSe$. A $2 \times 2 \times 2$ supercell was used to model W-disorder on Mo site with 24 atom cell (Mo = 4, W = 4, S = 16; and Mo = 4, W = 4, S = 8, Se = 8) atom per cell.

completely filled in $(Mo_{0.5}W_{0.5})S_2$ (Fig. 5a and b). This moves the bonding t_{2g} and e_g states (Fig. 6b and c) to E_F, where the majority of states belong to Mo/W/Ta t_{2g}-bands. Here, t_{2g} is a combination of d_{xy}, d_{yz}, and d_{xz} orbitals and e_g represents $d_{x^2y^2}$ and d_{z^2} orbitals. The S p-bands near E_F are situated in the same energy range as the Mo/W d-bands in $(Mo_{0.5}W_{0.5})S_2$ (Fig. 5b), and Ta causes reduced filling of S p-bands that also move closer to E_F. Thus, the crossover of partially-filled Mo/W-d and S-p bands at E_F caused by Ta predicts metallic behaviour of $(Mo_{0.4}W_{0.4}Ta_{0.2})S_2$.

In summary, our DFT results reveal that combining structurally different 1T-HfS_2 and 2H-MoS_2 phases stabilizes the heterostructured arrangement over solid-solution-like single-

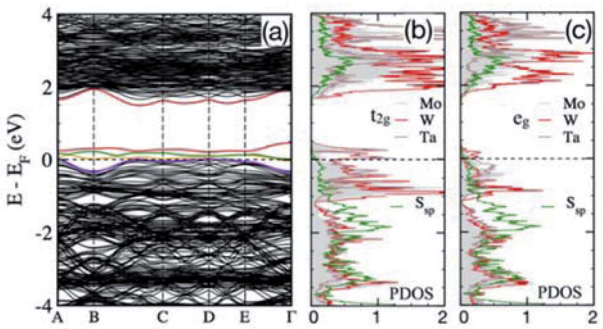

Fig. 6 Electronic band-structure (a), and Mo/W/Ta(t_{2g}, e_g)/S-sp partial density of states (states/eV-atom) (b, c) calculated for single-phase $(Mo_{0.4}W_{0.4}Ta_{0.2})S_2$. Presence of Ta at the metal site changes the semiconducting behavior of $(Mo_{0.5}W_{0.5})S_2$ to metallic in $(Mo_{0.4}W_{0.4}Ta_{0.2})S_2$. A $4 \times 4 \times 2$ supercell was used to model the 0.4 (Mo):0.4 (W):0.2 (Ta) disorder with 96 atom per cell (Mo = 13, W = 13, Ta = 6, S = 64).

phase (1T or 2H) states. At the same time, blending isostructural TMDCs, such as 2H-MoX_2 and 2H-WX_2 (X = S, Se), produces single-phase materials; even so, the metastable heterostructured intermediates are observed after the low-temperature stages of the previous experiments.[11] Doping group 6 TMDCs with a group 5 metal (Ta) is not expected to affect the phase stability of the resulting compounds, but it changes transport behaviour from semiconducting to metallic.

3.3 Electronic transport measurements

Electronic transport of the equimolar HfS_2/MoS_2 heterostructure and some previously prepared multi-principal element, single-phase TMDCs,[11] have been studied using photoconductivity, optical band gap, and electrical resistivity measurements. The experimental band gap values along with those predicted by the DFT calculations are summarized in Table 2, together with those reported in the literature.

The additional experimental details on measurements performed can be found in the ESI.† Several observations are worth noting. First, in the majority of the cases, the experimental values are in a good agreement with those predicted by DFT or published in the literature. The band gap values experimentally determined for both the HfS_2/MoS_2 and the multi-principal elements TMDCs shown in Table 2 are below those observed in the pure binary precursors, and obviously can be fine-tuned by altering the material's chemical and phase compositions.

The electronic transport behaviour of multi-principal element TMDCs can be further manipulated by doping with group 5 transition metals, such as Ta, that converts them from semiconductors into metallic-type conductors.[30] To illustrate this, we measured temperature dependence of the electrical resistivity, $\rho(T)$, of $W_{0.4}Mo_{0.4}Ta_{0.2}S_2$ using a Physical Property Measurements System (PPMS, Quantum Design, Inc.) employing a standard four-probe technique in magnetic field up to 120 kOe. The ρ *vs.* (T) measured during cooling and heating between 320 K and 1.8 K in the absence of magnetic field ($H = 0$) is shown in Fig. 7. Both the heating and cooling curves are practically identical. Consistent with the theoretical prediction, $W_{0.4}Mo_{0.4}Ta_{0.2}S_2$ demonstrates a weakly temperature-dependent metallic conductivity between 300 and 14 K. A minor increase in the resistivity observed at $T \leq 14$ K can be attributed to the presence of electron transport barriers between crystallites in the sample that reduce its overall conductivity at cryogenic temperatures. The electrical resistivity measured as a function of the magnetic field up to 120 kOe (Fig. 7, inset) indicates very weak but positive magnetoresistance of ~1.2% at $T = 1.8$ K without any sign of saturation.

Table 2 Indirect band gaps determined by photoconductivity and optical measurements

Sample	E_g, eV photoconductivity	E_g, eV optical (Tauc plot)	E_g, eV (DFT)
MoS_2	1.26	1.23 (lit.[26])	1.32
HfS_2	—	1.80 (lit.[27])	1.82
HfS_2/MoS_2	0.96	1.09	1.01
WS_2	—	1.35 (lit.[26])	1.15
WSe_2	1.20	1.20 (lit.[28,29])	1.36
$MoSe_2$	—	1.10 (lit.[27])	1.28
$Mo_{0.5}W_{0.5}S_2$	0.92	0.81	1.02
$Mo_{0.5}W_{0.5}SSe$	—	1.10	1.17

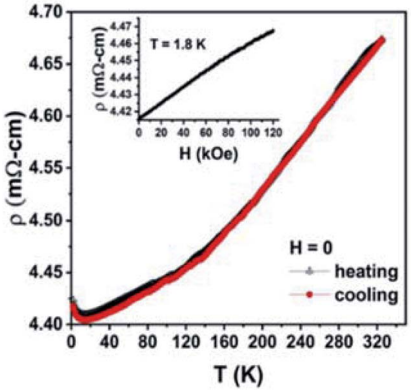

Fig. 7 Electrical resistivity of $W_{0.4}Mo_{0.4}Ta_{0.2}S_2$ as a function of temperature, measured at heating (black triangle), and cooling (red solid circle) in the absence of magnetic field. Inset shows resistivity as a function of the magnetic field up to 120 kOe at $T = 1.8$ K.

4 Conclusions

In contrast to the group 5 and 6 TMDCs, HfS_2 does not form a solid solution with MoS_2 after prolonged mechanical milling and annealing, even if they are performed in a cyclic manner. The misfit 3D-heterostructures formed from 1T-HfS_2 and 2H-MoS_2 building blocks show semiconducting behaviour with indirect band gap around 1 eV, which agrees well with the value predicted by DFT calculations and is lower than the values reported for the pure binary precursor materials. Our results also demonstrate that electronic transport in bulk TMDCs can be successfully manipulated using doping with appropriate refractory metals, which opens new avenues for engineering of vdW materials with tuneable physical properties.

Author contributions

I. Z. H., O. D. contributed to design of experiments, performed materials synthesis, materials characterization and contributed to interpretation of results; O. D. performed Rietveld refinements; S. Z. M., R. V. G and A. K. P. performed electronic transport experiments and data interpretation; V. K. P. contributed to structural data interpretation; P. S. and D. D. J. performed DFT calculations and analysis; V. P. B. conceived the idea, supervised and guided the study, contributed to design of experiments and data interpretation. All authors provided comments and edits during the preparation of the manuscript.

Conflicts of interest

There are no conflicts to declare.

Acknowledgements

The materials development was supported by the Ames Laboratory's Laboratory Directed Research and Development (LDRD) program. Theoretical design & analysis, structural and physical property characterization efforts were supported by the U.S. Department of Energy (DOE) Office of Science, Basic Energy Sciences, Materials Science & Engineering Division. Ames Laboratory is operated for the U.S. DOE by Iowa State University of Science and Technology under Contract No. DE-AC02-07CH11358. Theoretical calculations were conducted using the advanced computing resources provided by Texas A&M High-Performance Research Computing.

Notes and references

1 A. V. Kolobov and J. Tominaga, *Two-Dimensional Transition-Metal Dichalcogenides*, Springer International Publishing, Switzerland, 2016.
2 A. K. Geim and I. V. Grigorieva, *Nature*, 2013, **499**, 419–425.
3 K. S. Novoselov, A. Mishchenko, A. Carvalho and A. H. Castro Neto, *Science*, 2016, **353**, aac9439.
4 V. S. Pervov and E. V. Makhonina, *Russ. Chem. Rev.*, 2000, **69**, 481–489.
5 M. Serra and R. Tenne, *J. Coord. Chem.*, 2018, **71**, 1669–1678.
6 H. Taghinejad, M. Taghinejad, A. A. Eftekhar, Z. Li, M. P. West, M. H. Javani, S. Abdollahramezani, X. Zhang, M. Tian, T. Johnson-Averette, P. M. Ajayan, E. M. Vogel, S.-F. Shi, W. Cai and A. Adibi, *ACS Nano*, 2020, **14**, 6323–6330.
7 J. Joshi, T. Zhou, S. Krylyuk, A. V. Davydov, I. Žutić and P. M. Vora, *ACS Nano*, 2020, **14**, 8528–8538.
8 J. R. Brent, N. Savjani and P. O'Brien, *Prog. Mater. Sci.*, 2017, **89**, 411–478.
9 F. Lacopi, J. J. Boeckl and C. Jagadish, *Semiconductors and Semimetals. v. 95, 2D Materials*, Academic Press, Cambridge, San Diego, Oxford, London, 2016.
10 F. A. Cotton, G. Wilkinson, C. A. Murillo, M. Bochmann and R. Grimes, *Advanced Inorganic Chemistry*, Wiley, New York, 5th edn, 1988.
11 I. Z. Hlova, O. Dolotko, B. W. Boote, A. K. Pathak, E. A. Smith, V. K. Pecharsky and V. P. Balema, *Chem. Commun.*, 2018, **54**, 12574–12577.
12 O. Dolotko, I. Z. Hlova, A. K. Pathak, Y. Mudryk, V. K. Pecharsky, P. Singh, D. D. Johnson, B. W. Boote, J. Li, E. A. Smith, S. L. Carnahan, A. J. Rossini, L. Zhou, E. M. Eastman and V. P. Balema, *Nat. Commun.*, 2020, **11**, 1–10.
13 I. Song, C. Park and H. C. Choi, *RSC Adv.*, 2015, **5**, 7495–7514.
14 L. F. Mattheiss, *Phys. Rev. B: Condens. Matter Mater. Phys.*, 1973, **8**, 3719.
15 T. Roisnel and J. Rodriguez-Carvajal, *Mater. Sci. Forum*, 2001, **378**, 118–123.
16 G. Kresse and J. Furthmüller, *Phys. Rev. B: Condens. Matter Mater. Phys.*, 1996, **54**, 11169–11186.
17 G. Kresse and J. Furthmüller, *Comp. Mater. Sci*, 1996, **6**, 15.
18 J. P. Perdew, K. Burke and M. Ernzerhof, *Phys. Rev. Lett.*, 1996, **77**, 3865–3868.
19 P. E. Blochl, *Phys. Rev. B: Condens. Matter Mater. Phys.*, 1994, **50**, 17953–17979.
20 G. Kresse and D. Joubert, *Phys. Rev. B: Condens. Matter Mater. Phys.*, 1999, **59**, 1758–1775.
21 G. Roman-Perez and J. M. Soler, *Phys. Rev. Lett.*, 2009, **103**, 096102.
22 J. Klimes, D. R. Bowler and A. Michaelides, *Phys. Rev. B: Condens. Matter Mater. Phys.*, 2011, **83**, 195131.
23 J. Heyd, G. E. Scuseria and M. Ernzerhof, *J. Chem. Phys.*, 2006, **124**, 219906.
24 Z.-X. Hu, H. P. Lan and W. Ji, *Sci. Rep.*, 2014, **4**, 5036.
25 A. B. Naden, K. J. O'Shea and D. A. MacLaren, *Nanotechnology*, 2018, **29**, 165704.
26 K. Kobayashi and J. Yamauchi, *Phys. Rev. B: Condens. Matter Mater. Phys.*, 1995, **51**, 17085.
27 K. Terashima and I. Imai, *Solid State Commun.*, 1987, **63**, 315–318.
28 R. Coehoorn, C. Haas and R. de Groot R, *Phys. Rev. B: Condens. Matter Mater. Phys.*, 1987, **35**, 6203–6206.
29 A. Prakash and J. Appenzeller, *ACS Nano*, 2017, **11**, 1626–1632.
30 V. P. Balema, S. Padalkar, I. Z. Hlova, T. Lan, O. Dolotko, V. K. Pecharsky, D. D. Johnson, A. Pathak and P. Singh, *U.S. Pat. Appl. Publ.*, 2020, US 20200109479 A1 20200409.